Stability of fragmentation of a Bose-Einstein condensate in a double well

Master's thesis

Patrick Winkler

Supervisor
Dr. Axel U. J. Lode

Professor
Prof. Christoph Bruder

University of Basel

Department of Physics

Abstract

In the present thesis we study the fragmentation of a Bose-Einstein condensate and its stability in a double-well potential. We provide an analytical discussion as well as numerical results using the multiconfigurational time-dependent Hartree for bosons (MCTDHB) method which is first derived. We study the dependence of the excited fraction of particles of the system on the barrier height of the potential. A new regime for strong particle interaction is found, where the condensate does not fragment even for high barriers. We moreover discuss the evolution of a condensed state as the potential is dynamically transformed from a single to a double well, particularly for the systems in the newly found regime [Phys. Rev. Lett. **99**, 030402 (2007)]. We then discuss how this regime compares to the so called "counterintuitive" regime, where the final state is not the fragmented ground state of its system, even for very slow ramping times.

Contents

Chapter 1

Introduction

A Bose-Einstein condensate (BEC) is a state of bosons usually at very low temperatures. It was first considered for a gas of non-interacting bosons, which is described in many textbook of statistical mechanics, see e.g. [1, 2]. In this system, below a finite transition temperature T_C, a macroscopical fraction of all atoms occupy the single-particle quantum ground state. This phenomenon is a consequence of the symmetry of the wave function under the interchange of two identical bosons.

It was soon pointed out that a repulsive interparticle interaction favors the condensation into a single state, since it prevents fragmentation into several (almost) degenerate states [3]. Because single-particle states are not well-defined for interacting particles, a more general criterion for BEC was needed. Such a criterion was provided by Penrose and Onsager in 1956 [4].

A BEC is called fragmented if more than one quantum mechanical states are occupied by a macroscopic fraction of the system particles. This is in contrast to a simple (or coherent) BEC, where only the ground state is macroscopically occupied [3].

BECs serve as a versatile toolbox to study generic quantum systems and phenomena [5, 6] since they have been realized in trapped ultracold atomic gases [7–9] very close to absolute zero. They have also been intensively investigated in theoretical works [10–12]. A particularly interesting system is the splitting of a BEC when a single trap is deformed into a double well [13–15]. For interacting BECs this can lead to a transition from a condensed to a fragmented state [16]. Studying such systems helps us understand and ultimately manipulate many-body quantum states.

It is important to note that in the thermodynamic limit frequently taken in statistical approaches, condensation of the ideal Bose gas only occurs in three dimensions. For fewer dimensions the presence of an external potential is neces-

sary for condensation, although not all forms of potentials lead to BEC. Condensation has been rigorously proven in 2D and 3D traps for repulsive interactions [17]. Furthermore, it has been shown that finite particle number effects can lead to condensation of systems for which it otherwise ($N \to \infty$) would not be possible to do so, e.g. the 1D harmonic potential [18].

In this work, we study the ground state of bosons in a double-well and the dynamics of splitting a BEC initially in a single well with a time-dependent barrier. For this purpose we use the Multiconfigurational Time-Dependent Hartree for Bosons (MCTDHB) method to numerically solve the underlying many-body problem. We investigate the impact of the barrier height on the system, namely on the density, orbitals, occupations, one- and two-body correlation functions in real and momentum-space as well as its fragmentation. We find that, for high mean-field interaction strengths, fragmentation disappears for all barrier heights. We also study the adiabatic nature of the ramp-up procedure of the barrier. Interestingly, we find a counterintuitive regime [19], where the final state of the evolution of the BEC is not the previously found fragmented ground state, if the ramp-up process of the barrier is sufficiently slowly.

The work is structured as follows. In Chapter 2 we derive the equations of motion of the MCTDHB method and provide an analytical discussion of double-well potentials. In Chapter 3 we apply MCTHDB to a system in a one-dimensional double-well potential. We first study the ground state of a double-well system and subsequently investigate how this relates to the evolution of a state with an increasing barrier. An review of our results is provided in Chapter 4.

Chapter 2

Analytical discussion and numerical method

In this chapter we derive the equations of motion of the MCTDHB method and introduce some relevant quantities of interest. We also provide an analytical discussion of the many-body ground state in a double-well potential.

2.1 MCTDHB: A numerical method for the many-body problem

2.1.1 Hamiltonian

We start with the dimensionless time-dependent Schrödinger equation

$$\hat{H}\,|\psi\rangle = i\partial_t\,|\psi\rangle \tag{2.1}$$

where $|\psi\rangle$ denotes a state of N interacting structureless bosons. The many-body Hamiltonian $\hat{H}$ is assumed to be

$$\hat{H}(\mathbf{r}_1,\mathbf{r}_2,...,\mathbf{r}_n;t) = \sum_{j=1}^{N}\hat{h}(\mathbf{r}_j;t) + \sum_{i>j=1}^{N}\hat{W}(\mathbf{r}_j-\mathbf{r}_i;t). \tag{2.2}$$

Here $\hat{h}(\mathbf{r};t) = \hat{T}(\mathbf{r};t) + \hat{V}(\mathbf{r};t)$ is the one-body Hamiltonian containing a term $\hat{T}$ for kinetic and a term $\hat{V}$ for potential energy, whereas $\hat{W}(\mathbf{r}_j-\mathbf{r}_i;t)$ denotes the pairwise interaction between the ith and jth bosons.

We introduce a complete set of time-dependent orbitals $\{\phi_k(\mathbf{r};t)\}$, which are normalized and orthogonal at any time t:

$$\int \phi_k^*(\mathbf{r};t)\phi_j(\mathbf{r};t)\,\mathrm{d}\mathbf{r} = \delta_{jk}. \tag{2.3}$$

Furthermore we can introduce a set of bosonic annihilation operators $\hat{b}_k(t)$ corresponding to the respective orbitals,

$$\hat{b}_k(t) = \int \phi_k^*(\mathbf{r};t)\hat{\Psi}(\mathbf{r})\,\mathrm{d}\mathbf{r}, \tag{2.4}$$

where $\hat{\Psi}(\mathbf{r})$ is the field operator in second quantization.

The Hamiltonian can now be expressed in terms of the operators $\hat{b}_k$ and $\hat{b}_k^\dagger$:

$$\hat{H} = \sum_{k,q} h_{kq}\hat{b}_k^\dagger\hat{b}_q + \sum_{k,q,s,l} W_{ksql}\hat{b}_k^\dagger\hat{b}_s^\dagger\hat{b}_q\hat{b}_l. \tag{2.5}$$

Here h_{kq} and W_{ksql} are the matrix elements of the one-body Hamiltonian $\hat{h}$

$$h_{kq}(t) = \int \phi_k^*(\mathbf{r};t)\hat{h}(\mathbf{r})\phi_q(\mathbf{r};t)\,\mathrm{d}\mathbf{r}, \tag{2.6}$$

and the two-body operator $\hat{W}$

$$W_{ksql}(t) = \int\int \phi_k^*(\mathbf{r};t)\phi_s^*(\mathbf{r}';t)\hat{W}(\mathbf{r}-\mathbf{r}')\phi_q(\mathbf{r};t)\phi_l(\mathbf{r};t)\,\mathrm{d}\mathbf{r}d\mathbf{r}'. \tag{2.7}$$

So far all quantities have been dimensionless. To get a dimensional Hamiltonian of the same form, we substitute $r_i \to r_i = r_i L$ where L is a suitable length scale. Choosing $L = 1\mu$m and using the bosonic isotope $^{87}\mathrm{Rb}$, the time is expressed in units of $\frac{mL^2}{\hbar} = 1.37$ms and, correspondingly, the scale of energy is $\frac{\hbar^2}{mL^2} = 116$ Hz, where m denotes the mass of a single rubidium atom [20].

2.1.2 Derivation of equations of motion

In this section, we recapitulate the derivation of MCTDHB, as detailed in Ref. [20]. To solve the many-body Schrödinger equation, we use a multiconfigurational time-dependent ansatz,

$$|\psi\rangle = \sum_{\vec{n}} C_{\vec{n}}(t)\,|\vec{n};t\rangle, \tag{2.8}$$

$$\text{with } |\vec{n};t\rangle = \frac{1}{\sqrt{n_1!n_2!...n_M!}}\left[b_1^\dagger(t)\right]^{n_1}\left[b_2^\dagger(t)\right]^{n_2}...\left[b_M^\dagger(t)\right]^{n_M}|vac\rangle\,. \tag{2.9}$$

$\vec{n} = (n_1, n_2, ..., n_M)$ is an "occupation-number vector" of the M orbitals. Note that $n_1 + n_2 + ... + n_M = N$ is the total number of particles and is preserved.

$|\vec{n};t\rangle$ are the so called time-dependent permanents. The ansatz for the wave function in Eq. (2.8) is an exact expansion in the limit of $M \to \infty$, since the set of permanents then spans the whole Hilbert space. Practically the $M \to \infty$ limit is of course not possible to compute, and we need to reduce the size of the Hilbert space for realistic computations. This is where the advantage of allowing time-dependent permanents comes into effect; it allows us to greatly reduce the number of orbitals that have to be computed, while still retaining an accurate (i.e.,close to exact) description of the many-body system [21].

Further, we introduce the matrix elements of the reduced one-body and two-body density matrices

$$\rho_{kq} = \langle\psi|\, \hat{b}_k^\dagger \hat{b}_q \,|\psi\rangle\,, \tag{2.10}$$

$$\rho_{ksql} = \langle\psi|\, \hat{b}_k^\dagger \hat{b}_s^\dagger \hat{b}_q \hat{b}_l \,|\psi\rangle\,. \tag{2.11}$$

Using the above definitions, the functional action of the time-dependent Schrödinger equation [22] is given by

$$S[\{C_{\vec{n}}\},\{\phi_k(\mathbf{r};t)\}] = \int \mathrm{d}t \left(\langle\psi|\, \hat{H} - i\partial_t \,|\psi\rangle + \sum_{i,j} \mu_{ij}(t)(\langle\phi_i|\phi_j\rangle - \delta_{ij}) \right). \tag{2.12}$$

The $\mu_{ij}(t)$ are Lagrange multipliers, which are introduced to ensure the orthonormality of the orbitals $\phi_k(\mathbf{r};t)$ at all times t. Using the principle of stationary action [22] with respect to both sets of parameters, we can derive equations of motion using the usual Lagrangian formalism. A detailed derivation can be found e.g. in Ref. [20]. This leads to the following equation:

$$\boldsymbol{\mathcal{H}}(t)\mathbf{C}(t) = i\partial_t \mathbf{C}(t), \tag{2.13}$$

$$\text{where} \quad \mathcal{H}_{\vec{n}\vec{n}'}(t) = \langle\vec{n};t|\, \hat{H} - i\partial_t \,|\vec{n}';t\rangle\,, \tag{2.14}$$

$$\text{and} \quad i\,|\partial_t\phi\rangle = \hat{\mathbf{P}} \left(\hat{h}\,|\phi_j\rangle + \sum_{k,s,q,l}^{M} \rho_{jk}^{-1}\rho_{ksql}\hat{W}_{sl}\,|\phi_q\rangle \right), \tag{2.15}$$

$$\text{with} \quad \hat{\mathbf{P}} = 1 - \sum_{j}^{M} |\phi_j\rangle\,\langle\phi_j|. \tag{2.16}$$

Equation (2.13) defines a linear first-order differential equation in time. The matrix $\boldsymbol{\mathcal{H}}(t)$ depends on time, since it is composed of time-dependent permanents, which can be seen in Eq. (2.14). Furthermore Eq. (2.15) and (2.16)

describe a system of coupled non-linear differential equations. Importantly, Eq. (2.15) and (2.13) are coupled through the matrix elements h_{kq}, W_{ksql}, ρ_{kq} and ρ_{ksql}, see Eq. (2.6), (2.10) and (2.11).

2.1.3 Numerical implementation

We use a discrete variable representation (DVR) of N functions on a grid. The orbitals are represented by their values on the grid points x_α, i.e.,

$$\phi(x) \to \boldsymbol{\phi} = (w_1^{1/2}\phi(x_1), w_2^{1/2}\phi(x_2), ..., w_N^{1/2}\phi(x_N))^T, \tag{2.17}$$

where w_α are weights defined by the quadrature, for more details see e.g. Ref. [23].

We note here that the software implementation used, MCTDH-X, is freely available online [24]. It also implements the generalization of the method to fermionic systems which reflects in its name.

2.1.4 Quantities of interest

In the following we discuss some quantities necessary in order to analyze our system. As we, in this thesis, will only investigate one-dimensional systems in Chapter 3, the subsequent quantities are also restricted to the one-dimensional case. For a consistent notation, we replace $\mathbf{r}$ with x. First we look at the reduced one-body and two-body density matrices, which take on the form

$$\rho^{(1)}(x, x'; t) = \sum_{k,q}^{M} \rho_{kq}(t)\phi_k^*(x'; t)\phi_q(x; t) \quad \text{and} \tag{2.18}$$

$$\rho^{(2)}(x_1, x_2, x_1', x_2'; t) = \sum_{k,s,q,l}^{M} \rho_{ksql}(t)\phi_k^*(x_1'; t)\phi_s^*(x_2'; t)\phi_q(x_1; t)\phi_q(x_2; t). \tag{2.19}$$

We note the special case $x = x'$ for the reduced one-body density which leads to

$$\rho(x) = \sum_{k,q}^{M} \rho_{kq}(t)\phi_k^*(x; t)\phi_q(x; t). \tag{2.20}$$

which is simply called *density*.

Furthermore by choosing $x_1' = x_1$ and $x_2' = x_2$ in Eq. (2.19) we obtain the two-body density,

$$\rho^{(2)}(x_1, x_2) = \sum_{k,s,q,l}^{M} \rho_{ksql}(t)\phi_k^*(x_1;t)\phi_s^*(x_2;t)\phi_q(x_1;t)\phi_q(x_2;t). \tag{2.21}$$

A further quantity of interest is the *excited fraction*. It quantifies the fraction of bosons which do *not* occupy the eigenfunction of the reduced one-body density corresponding to its largest eigenvalue. Consequently, we need to determine the eigenvalues of the matrix-elements ρ_{kq}, which are called natural occupations $\rho_k^{(NO)}$ and are normalized to unity. This gives us the excited fraction

$$F = 1 - \rho_1^{(NO)}. \tag{2.22}$$

For a simple BEC $F \approx 0$, i.e.,only $\rho_1^{(NO)}$ is macroscopic. Generally a value of the excited fraction F significantly different from zero, however, does not necessarily imply a fragmented system. This can be the case when a large number of states are occupied microscopically. Since we will herein consider only two orbitals, we can directly use the excited fraction as a measure for the fragmentation.

We define the first-order and second-order normalized correlation functions as [25]:

$$g^{(1)}(x, x') = \frac{\rho^{(1)}(x, x')}{\sqrt{\rho^{(1)}(x, x)\rho^{(1)}(x', x')}} \quad \text{and} \tag{2.23}$$

$$g^{(2)}(x_1, x_2, x_1', x_2') = \frac{\rho^{(2)}(x_1, x_2, x_1', x_2')}{\sqrt{\rho^{(1)}(x_1, x_1)\rho^{(1)}(x_2, x_2)\rho^{(1)}(x_1', x_1')\rho^{(1)}(x_2', x_2')}}. \tag{2.24}$$

respectively. Analogously, one can define these correlations in momentum space. By applying a Fourier transform to the orbitals $\mathcal{F}(\phi_k(x;t)) = \tilde{\phi}_k(k;t)$ we obtain the reduced one-body and two-body densities in momentum space

$$\rho^{(1)}(k, k';t) = \sum_{k,q}^{M} \rho_{kq}(t)\tilde{\phi}_k^*(k';t)\tilde{\phi}_q(k;t), \tag{2.25}$$

$$\rho^{(2)}(k_1, k_2, k_1', k_2';t) = \sum_{k,s,q,l}^{M} \rho_{ksql}(t)\tilde{\phi}_k^*(k_1';t)\tilde{\phi}_s^*(k_2';t)\tilde{\phi}_q(k_1;t)\tilde{\phi}_q(k_2;t). \tag{2.26}$$

This leads to the correlation functions expressed in momentum space

$$g^{(1)}(k,k') = \frac{\rho^{(1)}(k,k')}{\sqrt{\rho^{(1)}(k,k)\rho^{(1)}(k',k')}}, \tag{2.27}$$

$$g^{(2)}(k_1,k_2,k_1',k_2') = \frac{\rho^{(2)}(k_1,k_2,k_1',k_2')}{\sqrt{\rho^{(1)}(k_1,k_1)\rho^{(1)}(k_2,k_2)\rho^{(1)}(k_1',k_1')\rho^{(1)}(k_2',k_2')}}. \tag{2.28}$$

The correlation functions $g^{(1)}$ and $g^{(2)}$ give a measure for the first and second-order coherence of the system. For $g^{(1)}(x,x') \approx 1$ [$g^{(2)}(x_1,x_2,x_1',x_2') \approx 1$] everywhere a system is approximately first- (second-) order coherent. If this is the case, the same needs to hold true analogously for the correlation functions in momentum space as well, i.e.,$g^{(1)}(k,k') \approx 1$ [$g^{(2)}(k_1,k_2,k_1',k_2') \approx 1$]. The same is also true in reverse. [20].

The second-order correlation functions depend on four parameters and are therefore hard to visualize. For this reason, we will only plot the diagonal elements $g^{(2)}(x_1,x_2,x_1,x_2)$ and $g^{(2)}(k_1,k_2,k_1,k_2)$, respectively. By restricting ourselves to diagonal terms we, however, cannot conclude with certainty that the system is second-order coherent, even if $g^{(2)} \approx 1$ everywhere in the plot [20]. More detailed studies in the full (x_1,x_2,x_1',x_2') space are needed.

2.2 Fragmentation in a double-well potential

In this section we show analytically how fragmentation of the ground state can occur in a double-well potential [26, 27].

2.2.1 Model

We start by simplifying the general ansatz of the many-body wave function of Eq. (2.8) to a single permanent,

$$|\psi_{s/d}\rangle = |\vec{n}\rangle\,, \tag{2.29}$$

where the permanent $|\vec{n}\rangle$ is defined in Eq. (2.9). Since we are only interested in the ground state, we will drop all time-dependencies for the remainder of this section. Furthermore we will only consider the special cases of $M = 1$ and

$M = 2$ orbitals. For the single-orbital case ($M = 1$) our ansatz for the N-body wave function is now reduced to the Hartree-Fock state

$$|\psi_s\rangle = |N\rangle = \frac{1}{\sqrt{N!}}\left[b_0^\dagger\right]^N |vac\rangle = \frac{\left(\int \phi_0(\mathbf{r})\hat{\Psi}^\dagger(\mathbf{r})\,\mathrm{d}\mathbf{r}\right)^N}{\sqrt{N!}}|vac\rangle\,, \tag{2.30}$$

which we will also refer to as *single* (or *coherent*) *condensate*. For two orbitals the state now explicitly reads

$$|\psi_d\rangle = |N_1, N_2\rangle = \frac{\left(\int \phi_0(\mathbf{r})\hat{\Psi}^\dagger(\mathbf{r})\,\mathrm{d}\mathbf{r}\right)^{N_1}}{\sqrt{N_1!}}\frac{\left(\int \phi_0(\mathbf{r})\hat{\Psi}^\dagger(\mathbf{r})\,\mathrm{d}\mathbf{r}\right)^{N_2}}{\sqrt{N_2!}}|vac\rangle\,, \tag{2.31}$$

where $N_1 + N_2 = N$. In the following, we will refer to states of this form as *dual condensates*.

2.2.2 Analysis of energies

We now consider a system of N interacting bosons in an arbitrary external potential as described by the Hamiltonian given in Eq. (2.6). The interparticle interaction is chosen to be a repulsive contact interaction

$$\hat{W}(\mathbf{r}_j - \mathbf{r}_i) = \lambda_0\delta(\mathbf{r}_j - \mathbf{r}_i), \tag{2.32}$$

with $\lambda_0 \geq 0$. Under the assumption that all orbitals are real, we find the expectation value of the energy (Gross-Pitaevskii energy[28]) for a single condensate $|\psi_s\rangle$,

$$E_s = N\epsilon(\phi_0) + \frac{1}{2}\lambda_0 N(N-1)\int \phi_0^4(\mathbf{r})\,\mathrm{d}\mathbf{r}, \tag{2.33}$$

where $\epsilon(\phi) = \int \phi(\mathbf{r})\hat{h}\phi(\mathbf{r})d\mathbf{r}$ is the single-particle energy of the orbital $\phi(\mathbf{r})$. For the dual condensate $|\psi_d\rangle$

$$\begin{aligned} E_d =& N_1\epsilon(\phi_1) + N_2\epsilon(\phi_2) + \frac{1}{2}\lambda_0 N_1(N_1-1)\int \phi_1^4(\mathbf{r})\,\mathrm{d}\mathbf{r} \\ &+ \frac{1}{2}\lambda_0 N_2(N_2-1)\int \phi_2^4(\mathbf{r})\,\mathrm{d}\mathbf{r} + 2\lambda_0 N_1 N_2\int \phi_1^2(\mathbf{r})\phi_2^2(\mathbf{r})\,\mathrm{d}\mathbf{r}, \end{aligned} \tag{2.34}$$

We now further assume that both condensates have approximately the same density everywhere, i.e.,$N_1\phi_1^2(\mathbf{r}) + N_2\phi_2^2(\mathbf{r}) \simeq N\phi_0^2(\mathbf{r})$. This implies that the single-particle energies ϵ of the condensates are approximately equal. Moreover, for a

large number of particles N, the quadratic terms of the interaction energy will dominate. We find

$$E_s^{quad} = \frac{1}{2}\lambda_0 N^2 \int \phi_0^4(\mathbf{r})\,\mathrm{d}\mathbf{r}, \tag{2.35}$$

$$E_d^{quad} \simeq \frac{1}{2}\lambda_0 N^2 \int \phi_0^4(\mathbf{r})\,\mathrm{d}\mathbf{r} + \lambda_0 N_1 N_2 \int \phi_1^2(\mathbf{r})\phi_2^2(\mathbf{r})\,\mathrm{d}\mathbf{r}. \tag{2.36}$$

Evidently, there is an extra term in the interaction energy of the dual condensate. This additional contribution to the energy was first identified by Nozières [3] and used as an argument against the fragmentation of condensates. This argument, however, works only under the assumption that $\phi_1(\mathbf{r})$ and $\phi_2(\mathbf{r})$ have a substantial density overlap. If the density overlap is negligible, the additional quadratic term in interaction energy of the dual condensate in Eq. (2.36) in comparison to the energy of a single condensate Eq. (2.35) vanishes. Therefore, to determine which configuration is energetically more favorable we now must also analyze terms of the interaction energy linear to N,

$$E_s^{lin} = -\frac{1}{2}\lambda_0 N \int \phi_0^4(\mathbf{r})\,\mathrm{d}\mathbf{r}, \tag{2.37}$$

$$E_d^{lin} = -\frac{1}{2}\lambda_0 N_1 \int \phi_1^4(\mathbf{r})\,\mathrm{d}\mathbf{r} - \frac{1}{2}\lambda_0 N_2 \int \phi_2^4(\mathbf{r})\,\mathrm{d}\mathbf{r}. \tag{2.38}$$

2.2.3 Emergence of fragmentation

We will now show how the above contributions favors the dual condensate when in a double-well potential. Consider an arbitrary symmetrical double-well potential, with a double minimum along the x-axis. We will focus on the limiting case of an infinitely strong barrier, which results in all states having zero amplitudes at $x = 0$. Together with the symmetry of the system, this implies that the ground state of the single condensate is twofold degenerate. A symmetric and an antisymmetric solution exist, i.e.,

$$\phi_{s/a}(x, y, z) = \pm\phi_{s/a}(-x, y, z), \tag{2.39}$$

with exactly the same single-particle energy $\epsilon = \langle\phi|\, H\, |\phi\rangle$. Using the symmetric and antisymmetric wave functions, we can construct two new wave functions

$$\phi_{l/r}(\mathbf{r}) = \frac{1}{\sqrt{2}}[\phi_s(\mathbf{r}) \pm \phi_a(\mathbf{r})], \tag{2.40}$$

which are strictly confined to the left and to the right well of the potential. Using these two wave functions as orbitals for our dual condensate ansatz with $N_1 = N_2 = N/2$ and using the fact that $\phi_s^2 \equiv \phi_a^2$ it is easy to calculate the single-particle energy as well as the quadratic terms of the interaction energy. We find that Eqs. (2.35) and (2.36) are the same for both the single and the dual condensate. However, calculating the linear contribution of the interaction energy in Eq. (2.37) of the single condensate and comparing it to Eq. (2.38) we find

$$\begin{aligned} E_d^{lin} &= -\frac{1}{2}\lambda_0 N_1 \int (\frac{1}{\sqrt{2}}[\phi_s(\mathbf{r}) + \phi_a(\mathbf{r})])^4 d\mathbf{r} - \frac{1}{2}\lambda_0 N_2 \int (\frac{1}{\sqrt{2}}[\phi_s(\mathbf{r}) - \phi_a(\mathbf{r})])^4 \,\mathrm{d}\mathbf{r} \\ &= -\frac{1}{2}\lambda_0 (N_1 + N_2) \int \frac{1}{4}(\phi_s^4(\mathbf{r}) + 6\phi_s^2(\mathbf{r})\phi_a^2(\mathbf{r}) + \phi_a^2(\mathbf{r}))\,\mathrm{d}\mathbf{r} \\ &= -\lambda_0 N \int \phi_s^4(\mathbf{r})\,\mathrm{d}\mathbf{r} \\ &= 2E_s^{lin}. \end{aligned} \tag{2.41}$$

Since this term is strictly negative we have $E_s^{lin} < E_d^{lin}$. The dual (fragmented) condensate is energetically favorable overall, if the orbitals can be written as in Eq.(2.40). The orbitals $\phi_{l/r}$ have, however, a higher single-particle energy than $\phi_{a/s}$ because they are more localized. A sufficiently high interaction strength is therefore necessary for the dual condensate to overcome this additional cost.

Solutions of the many-body problem calculated with the MCTDHB method might differ from the solution provided in this section, even if we restrict it to $M = 2$ orbitals. The ansatz for the wave-function used with MCTDHB [Eq. (2.8)] is more general and allows the occupation of multiple permanents.

Chapter 3

Numerical results

This chapter provides an application of the previously derived MCTDHB method. In Section 3.1 we study the fragmentation in a double-well potential. In Section 3.2 we study a dynamical system with a barrier increasing in time.

3.1 Ground state

3.1.1 Double-well potential

We restrict ourselves to the one-dimensional case, i.e.,$\mathbf{r} = x$ and $\mathbf{k} = k$, and $M = 2$ orbitals for simplicity. It has been shown that two orbitals are sufficient to adequately describe the many-body physics of a fragmented condensate in a double-well [21]. We use a discrete variable representation (as mentioned in Section 2.1.3) of 256 functions on a grid of extent from -12 to 12. To ensure convergence, we checked that the density at the edge of the grid was always less than 10^{-10}. Furthermore we ensured that the relative energy difference to be smaller than 10^{-10} between 256 and 512 functions. We investigate the ground state of N bosons in an harmonic trap with a Gaussian shaped barrier,

$$\hat{V}(x) = \frac{x^2}{2} + V_0 \exp\left(-\frac{x^2}{2\sigma^2}\right). \tag{3.1}$$

Here, we choose $\sigma = 2$. See Figure 3.1 for a visualization of the potential for different barrier heights V_0. The kinetic energy is defined as $\hat{T}(x) = \frac{1}{2}\partial_x^2$. V_0 denotes the time-independent height of the Gaussian barrier. We choose the repulsive contact interaction

$$W(x_i - x_j) = \lambda_0 \delta(x_i - x_j), \tag{3.2}$$

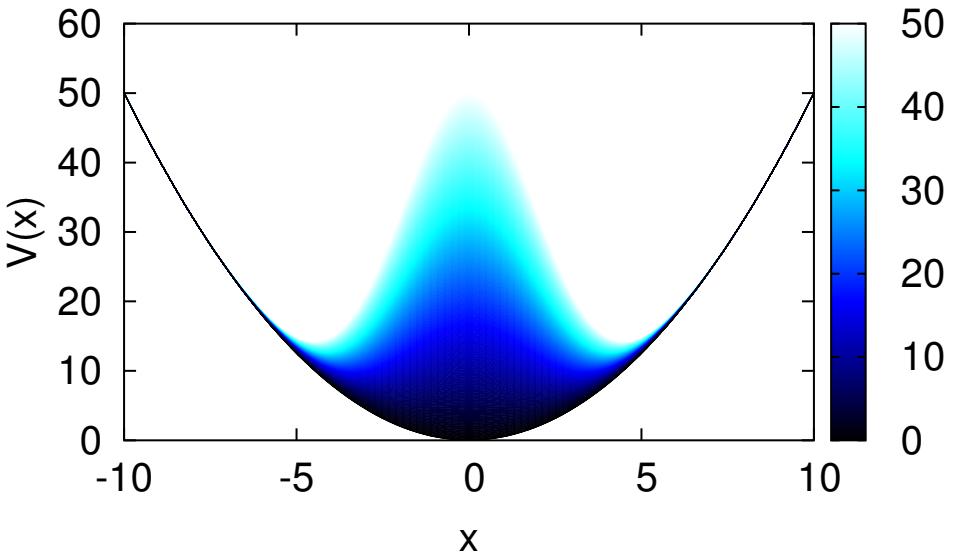

Figure 3.1 Illustration of the external potential. The shown potentials correspond to barrier a barrier thickness of $\sigma = 2$. Note that the minima of the potentials are shifted upwards from 0 as V_0 increases.

where $\lambda_0 = 0.1$ is the interaction strength. We will continue with an investigation of the system behavior as a function of the barrier height V_0 and the number of bosons N.

3.1.2 Eigenfunctions of the double-well potential

In the top row of Fig. 3.2 the first (left) and second (right) natural orbital are shown as a function of the barrier height. They are symmetric and antisymmetric, respectively. For small barriers the second orbital is almost 0 where the potential is minimal, in contrast to the first orbital which has the shape of a Gaussian. Its node also causes a greater kinetic energy $\langle\phi_2|\,\hat{T}\,|\phi_2\rangle$ of the second orbital, since it is proportional to the second derivative of the orbital. Both effects lead to a higher value for the single-particle energy of the second natural orbital $h_{22} = \langle\phi_2|\,\hat{h}\,|\phi_2\rangle$ compared to the first one $h_{11} = \langle\phi_1|\,\hat{h}\,|\phi_1\rangle$. This also explains why the occupation of the second orbital is very small in the case of small barriers, since the interaction between atoms is weak and not sufficient to render occupying the higher lying state energetically favorable.

For finite barrier heights, the first natural orbital develops a local minimum at

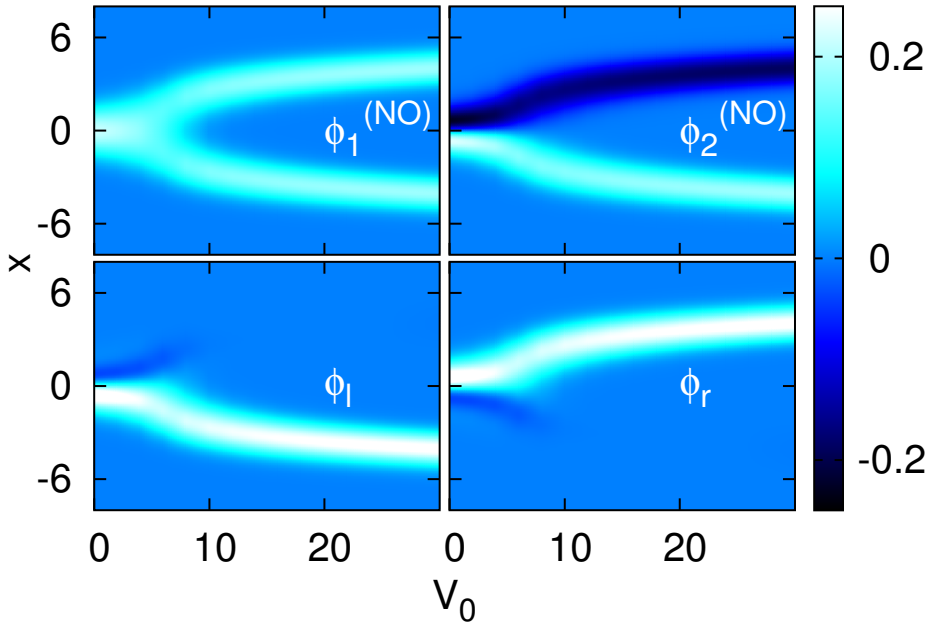

Figure 3.2 Density of different orbitals as a function of the position x and the barrier height V. In the top row ϕ_1^{NO} (left) and ϕ_2^{NO} (right) are plotted. In the bottom row two superpositions of these orbitals are plotted, namely $\phi_l = \frac{1}{\sqrt{2}}(\phi_1^{NO} + \phi_2^{NO})$ (left) and $\phi_r = \frac{1}{\sqrt{2}}(\phi_1^{NO} - \phi_2^{NO})$ (right). With increasing barrier height these orbitals are getting fully localized in one of the wells each. In consequence there is no overlap between the two orbitals and a fully fragmented state can be energetically favorable.

the center of the barrier to minimize the potential energy. Therefore, we have a decreasing energy gap $\Delta\epsilon = \langle\phi_1|\,\hat{h}\,|\phi_1\rangle - \langle\phi_2|\,\hat{h}\,|\phi_2\rangle$ for increasing barrier heights. This single-particle picture does not explain why the fragmentation of the system happens. The reason lies in the interaction energy, which can be decreased by occupying natural orbitals with higher energy, leading to an overall favorable energy configuration for the fragmented state [20]. This can be seen with the ansatz using two localized orbitals $\phi_l = \frac{1}{\sqrt{2}}(\phi_1^{NO}+\phi_2^{NO})$ and $\phi_r = \frac{1}{\sqrt{2}}(\phi_1^{NO}-\phi_2^{NO})$. For high barriers, these two orbitals are almost completely spatially separated in each well, i.e.,there is no overlap of the orbitals. As discussed in Sec. 2.2, this configuration is favorable for a fragmented BEC and our numerical results are consistent with this analytical model (compare Fig. 3.2 bottom row). Note that an ansatz with the particles being equally distributed between ϕ_l and ϕ_r is not actually the solution of the many-body Hamiltonian, which can be seen from the fact that spatially separated orbitals are not the natural orbitals. Therefore the simplification in our model (Sec. 2.2 and [26]) to describe the many-body wave function with only one permanent is not able to perfectly explain the physics of

this system.

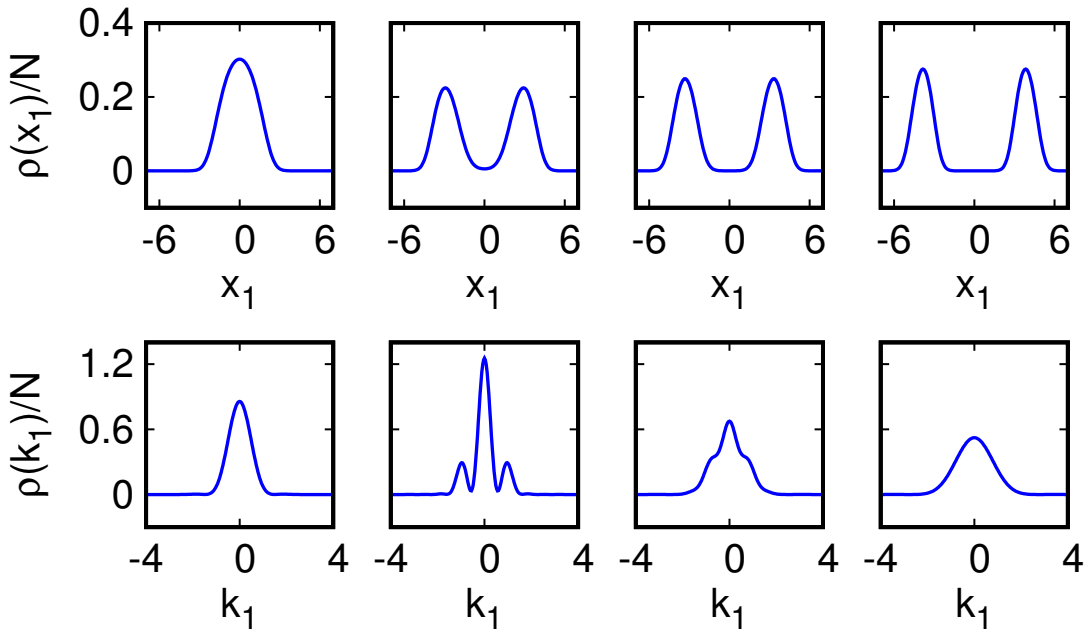

Figure 3.3 Density (upper row) and momentum density (lower row) for barrier heights 0, 12, 16, 25 from left to right. With increasing barrier height the density splits into two parts, localized in each well. The momentum density is Gaussian-like for both very low and high barrier height, but is modulated by an oscillation during the transition to fragmentation.

The first row of Fig. 3.3 shows the one-particle density at different barrier heights. It changes from a single Gaussian-like peak in the purely harmonic potential to two separate peaks, which are increasingly separated from each other. It is, however, not possible to infer fragmentation from the density alone.

In the second row the one-particle momentum distribution is shown. It starts with a Gauss-like distribution at $V_0 = 0$. At $V_0 = 12$ an oscillatory pattern is developed as the system spreads out over two wells. At the maximum considered barrier height of $V_0 = 25$, the distribution again takes the form of a Gaussian, but broader than the one of the state with $V_0 = 0$. This can be explained with the two narrower peaks of the position space density distribution, compared to the broader peak at $V_0 = 0$, since both are connected through Fourier transformation [20].

In Fig. 3.4 both the first and second-order coherence are shown, for the same barrier heights as in Fig. 3.3. To avoid numerical errors, the coherence is only plotted in regions where the density is bigger than 0.1%. The same rule is later

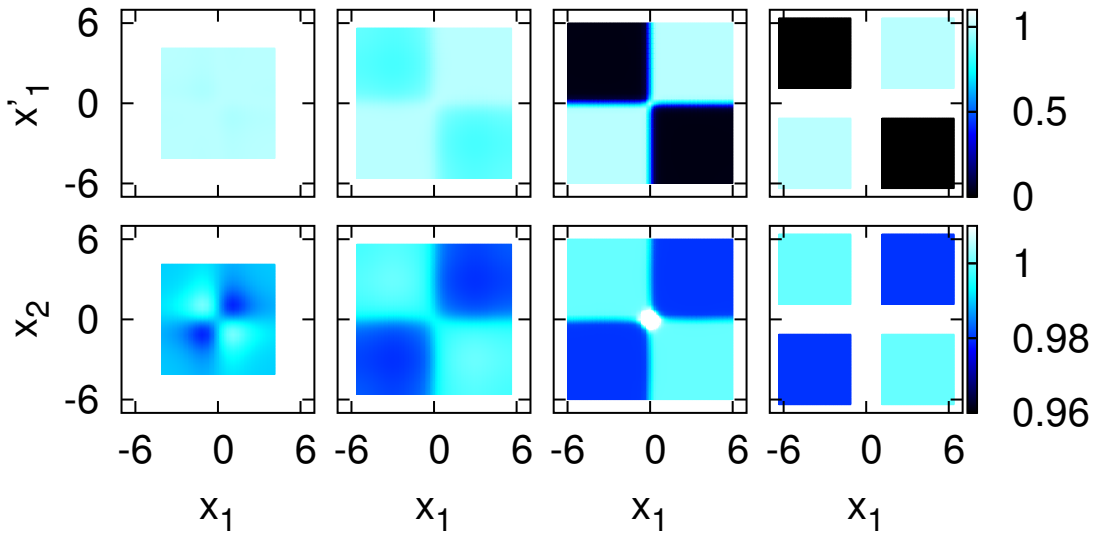

Figure 3.4 First and second-order correlation functions $|g^{(1)}(x_1, x_1')|^2$ and $g^{(2)}(x_1, x_2, x_1, x_2)$ (upper and lower row, respectively) in real space for barrier heights 0, 12, 16, 25 from left to right. In the first order coherence a transition from an initially coherent condensate to two first order incoherent samples happens between barrier heights 12 and 16. In contrast, the second-order coherence remains close to 1 at all barrier heights.

applied to the correlation functions in momentum space in Fig. 3.5. For $V_0 = 0$, the harmonic trap, the first order coherence $|g^{(1)}(x_1, x_1')|^2$ is very close to 1 for the whole system, i.e., it is coherent to first order. At a barrier height of $V_0 = 12$ the coherence between the two opposing peaks is already slightly decreased, whereas the peaks stay coherent within themselves. For even higher barriers the coherence between the peaks further decreases towards 0.

The second row of Fig. 3.4 shows the second-order coherence of the system. It stays close to 1 for all barrier heights. This, however, does not mean that our system is second-order coherent, since $g^{(2)}(x_1, x_2, x_1, x_2)$ only captures the values on the diagonal. Therefore, off-diagonal values could still be vastly different from 1.

In Fig. 3.5 first and second-order coherence are shown, but this time in momentum space. Only barrier heights of $V_0 = 0, 25$ are plotted. It is seen that first and second-order coherence of the system is lost for high barrier heights (Fig. 3.5, right column). Note that $g^{(2)}(k_1, k_2, k_1, k_2)$ depends on all values of $\rho^{(2)}(x_1, x_2, x_1', x_2')$, and therefore provides us with additional information about the off-diagonal terms of $g^{(2)}(x_1, x_2, x_1', x_2')$ which we do not see in Fig. 3.4 [20].

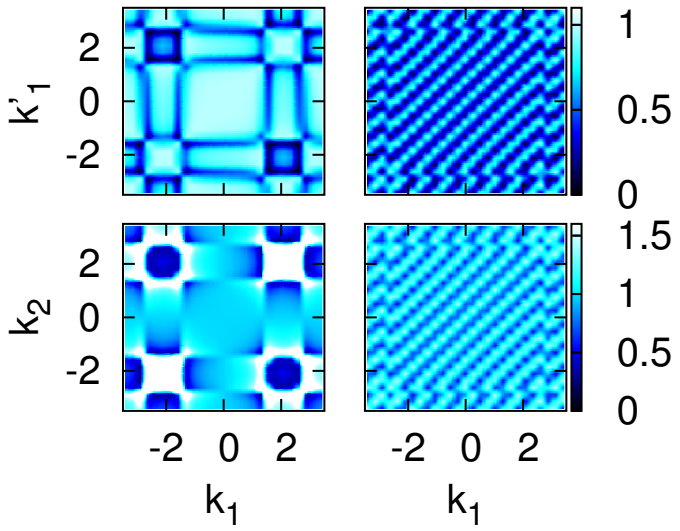

Figure 3.5 Same graph as Fig. 3.4 in momentum space (upper row $|g^{(1)}(k_1, k_1')|^2$ and lower row $g^{(2)}(k_1, k_2, k_1, k_2)$, with barrier heights of $V_0 = 0$ in the left column and $V_0 = 25$ in the right one. Both first and second-order coherence exhibit complex patterns. At a barrier height $V_0 = 0$, the condensate is almost coherent around the center of the potential. This coherence is lost at $V_0 = 25$ for both first and second-order coherence.

3.1.3 Disappearance of fragmentation

We now consider the same system with not only as a function of the barrier height, but also as a function of the number of particles. The results are plotted in Fig. 3.6. From this plot we can identify four distinct regions with different characteristics:

I In the region with small particle numbers and low barrier height, the orbitals are still similar to the single-particle solutions of the harmonic potential. In the single-particle picture, most particles populate the ground state while the first excited state is only very sparsely populated due to its higher kinetic energy and thus the condensate is coherent.

II In this region with moderate barrier heights and/or higher particle numbers, we still find one orbital to be much more populated than the other, i.e., the condensate is not fragmented. In contrast to region I, however, the less populated orbital has a lower single-particle energy $\epsilon_2 = \langle\phi_2|\,\hat{h}\,|\phi_2\rangle$. There are two factors that make this possible. First, the higher the barrier the smaller the energy gap is between the first and second single-particle eigenstates of the system. Second, in systems with more particles the over-

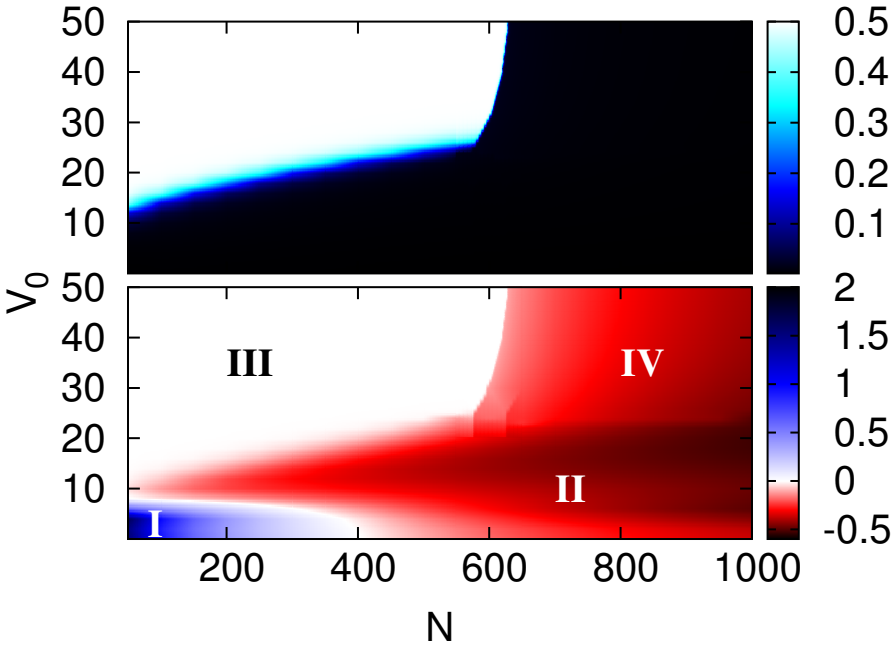

Figure 3.6 Fragmentation as a function of particle number N and barrier height V_0 (top) and difference of the one-particle energies h_{11} and h_{22} in units of h_{11} as a function of particle number N and barrier height V_0 (bottom). Comparing both plots it is apparent that for fragmented states the energy difference vanishes. A transition is visible inside the simple BEC for high particle numbers: at a barrier height where we would expect the condensate to fragment when extrapolating from lower particle numbers, the second orbital has lower one-particle energy for sufficient barrier heights and interaction energies. See text for further discussion.

all interaction energy gets proportionally bigger. The form of the highly populated orbital therefore increasingly deviates from an eigenstate of the single-particle Hamiltonian to also lower the interaction energy, at the cost some of some additional single-particle energy.

III For high barriers, the single-particle ground state of the double-well is almost twofold degenerate. As discussed earlier in Section 2.2, the ground state of the condensate is fully fragmented in this case, which we also find numerically. There is, however, an important difference between the analytical and the numerical solution. Namely, in contrast to the analytical solution, the orbitals are not spatially separated, but rather are just symmetric and antisymmetric versions of each other. The ansatz with only one permanent does not work with these orbitals, since they overlap and therefore would have a higher energy than the single condensate. To see how this solution is actually energetically favorable, one would need to analyze

how the coefficients $C_{\vec{n}}$ in Eq. (2.8) are structured. This difference also explains why the transition between Region II and Region III is somewhat smooth rather than instantaneous, which one would expect due to the totally different nature of the spatially fragmented state. But considering the numerical solution we get the following picture for the transition: With increasing barrier height the difference between the single-particle states gets smaller. Since the highly populated orbital is deformed to lower the interaction energy, the second orbital actually has a lower single-particle energy. It becomes therefore more and more energetically favorable to populate the second orbital.

IV The fourth region emerges for high barrier heights and particle numbers. Intuitively we would expect the ground state to be fragmented here based on the results with fewer particles and our analytical model. Numerically, however, we find that the ground state is of similar nature as in Region II. This indicates that the analytical model cannot be applied to regions where the mean-field interaction is very strong.

Regimes I-IV provide a complete characterization of the fragmentation of one-dimensional BEC in double-wells. See also complementary results on the system in Appendix A.

3.2 Dynamics

3.2.1 Potential

In this section we consider a double-well potential with a time-dependent barrier. For that purpose, we change the potential as defined in Eq. 3.1 to include a barrier with a time-dependent height $h(t)$:

$$\hat{V}(x,t) = A\frac{x^2}{2} + V_0 h(t) \exp\left(-\frac{x^2}{2\sigma^2}\right), \tag{3.3}$$

$$h(t) = \begin{cases} t/T_{ramp} & t < T_{ramp} \\ 1 & t \geq T_{ramp} \end{cases}. \tag{3.4}$$

First, we look at a system with $A = 1$ and $\sigma = 2$ for different barrier heights V_0 and ramp times T_{ramp}. For any fixed time t Eq. (3.3) thus is equivalent to potentials in the form of Eq. (3.1) that were discussed in Sec. 3.1. We also use

the same contact interaction as in Sec. 3.1 with $\lambda_0 = 0.1$. This allows us to directly compare resulting states after the ramping up of the barrier with the already examined ground states.

3.2.2 General results

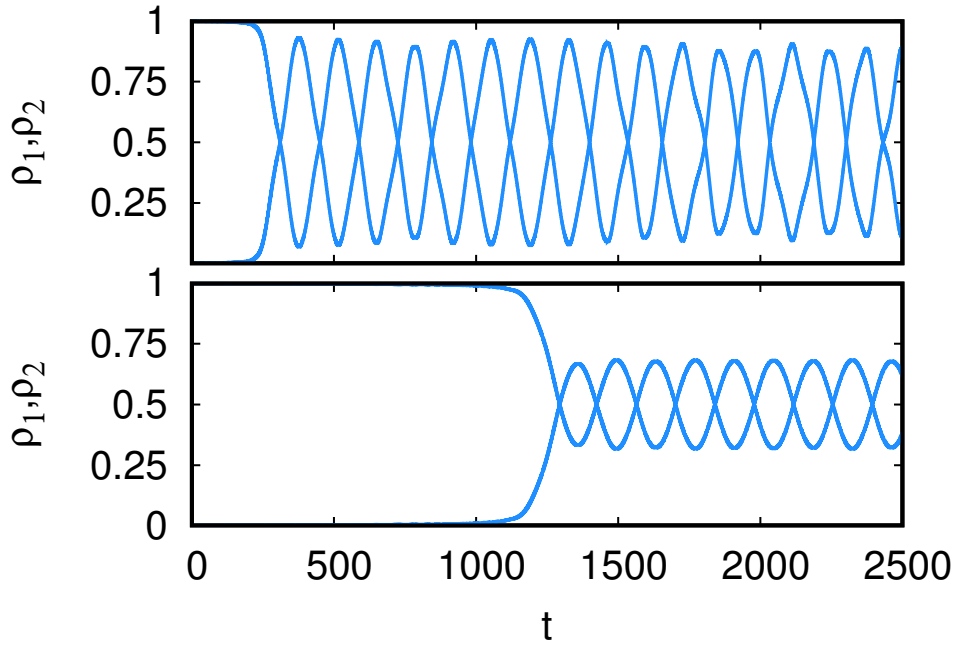

Figure 3.7 Natural occupation numbers $\rho_1(t)$ and $\rho_2(t)$ as a function of time for the ramp times 300 (top) and 1500 (bottom) in a system with $N = 500$ bosons and barrier height $V_0 = 30$. The state approaches the ground state of the double-well potential, which has $\rho_1 \approx \rho_2 \approx 0.5$. There are, however, signification oscillations even for $T_{ramp} = 1500$.

In Fig. 3.7 we can see the evolution of the natural occupation number as a function of time for the ramp times 300 and 1500 in a system with $N = 500$ bosons. We start with a slightly depleted BEC, $\rho_1(0) = 99.79\%$ and $\rho_2(0) = 0.21\%$. From there on, $\rho_2(t)$ increases continuously until the state becomes twofold fragmented. The occupation numbers, however, continue to oscillate around $\rho_1 \approx \rho_2 \approx 0.5$, which indicates that the system is not in the ground state [20].

Significant oscillations are still visible for $T_{ramp} = 1500$. This T_{ramp} corresponds to 2.06 s for a system composed of $^{87}\mathrm{Rb}$ atoms. This is already on the order of the lifetime of a BEC [14], but still is far from being ideally adiabatic.

We now consider systems with $N = 600$ bosons and a maximal barrier height

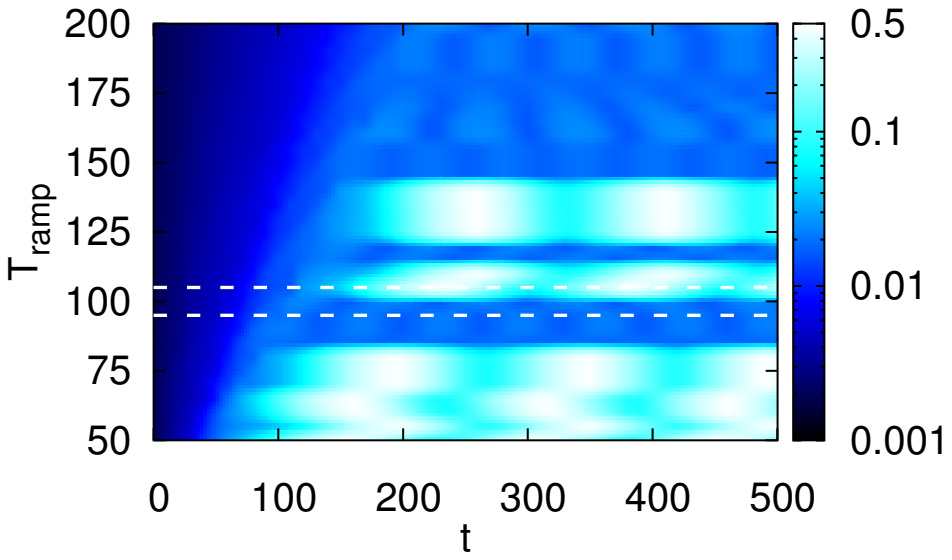

Figure 3.8 Excited fraction as a function of time t for different ramp-up times T_{ramp}, and constant $V_0 = 30$ and $N = 600$. For fast ramp-up times the resulting state oscillates around a fully fragmented state, while for slow times the system remains in the coherent ground state with only small fragmentations. For intermediate ramp-up times the behavior is chaotic, as the system ends up in either one of these states even for small changes of T_{ramp}. The white dashed lines indicate the time evolutions plotted in Fig 3.9.

of $V_0 = 30$. The resulting excited fractions are plotted in Fig. 3.8 as a function of t and T_{ramp}. For relatively large ramp times the state again approaches the ground state of the resulting double-well system, which in this case is not fragmented. As in the previous case, oscillations of a magnitude of roughly 1% are present.

For relatively fast ramp-up times ($T_{ramp} \approx 50$), the evolution of the system looks similar to the ones plotted in Fig. 3.7. The excited fraction of the initially only slightly depleted cased increases as the barrier is ramped up, and ends in a fully fragmented configuration with oscillations. This fragmented state is not the ground state of the system, but rather an excited state with a slightly higher energy. Because the barrier is ramped up quickly, we add additional energy to the system; as seen in Fig. 3.7 the amount is substantial and we are far away from the adiabatic regime. This added energy is larger than the energy difference between the ground state and a fully fragmented excited state which explains the behavior.

Interestingly there is no single ramp-up time at which the system switches

between the two behaviors as one naively could expect. Rather it changes multiple times as the ramp-up time is increased. To illustrate this, the time-evolution of natural occupation numbers for two specific configurations with $T_{ramp} = 95$ and $T_{ramp} = 105$ are plotted in Fig. 3.9. Note that it is the state with the higher ramp-up time $T_{ramp} = 105$ which tends towards the fully fragmented state, while the state with $T_{ramp} = 95$ remains in the coherent ground state with only small oscillations. The reasons for this to be possible likely lies within the small oscillations which occur during the ramp-up of the barrier. Depending on the height of the barrier at a specific point the oscillations can be amplified, providing the additional energy to deviate from the ground state.

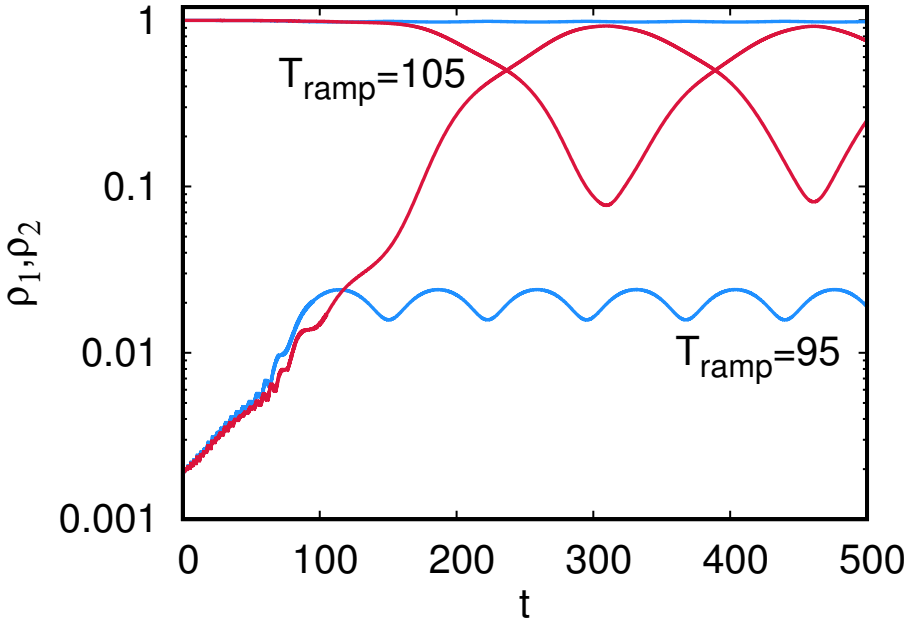

Figure 3.9 Natural occupation numbers $\rho_1(t)$ and $\rho_2(t)$ as a function of time for the ramp times 95 (blue) and 105 (red) in a system with $N = 600$ bosons and barrier height $V_0 = 30$, which corresponds to two horizontal lines in Fig. 3.8. Counter-intuitively a state with the faster ramp time $T_{ramp} = 95$ oscillates around the coherent ground state, while $T_{ramp} = 105$ oscillates around an excited, fragmented state.

3.2.3 Inverse regime

We now consider a similar system with $A = 0.5$ and a stronger interaction, $\lambda = 0.35$. The results for $T_{ramp} = 25, 500$ are plotted in Fig. 3.10. In the case of $T_{ramp} = 25$ there is no significant qualitative difference to the system ex-

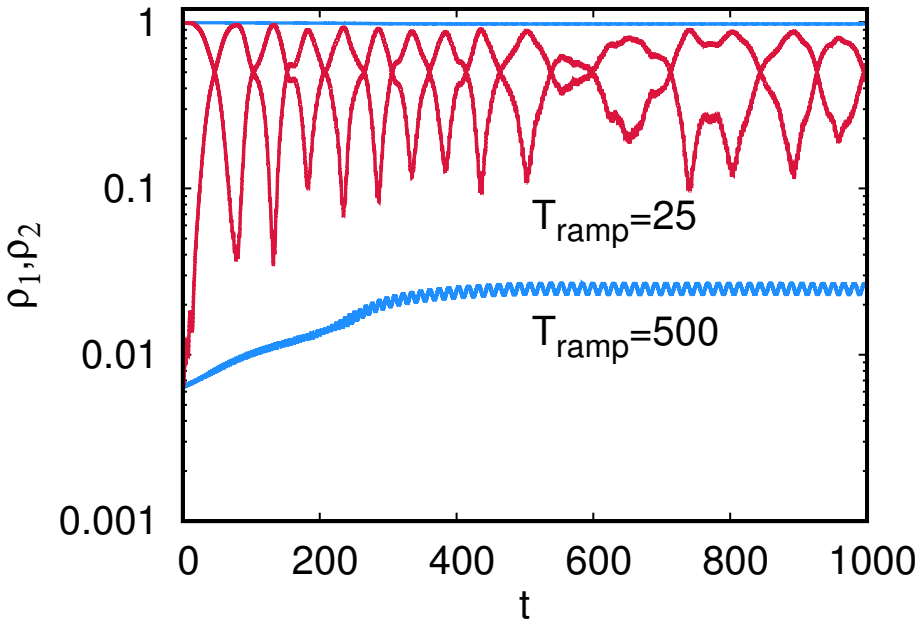

Figure 3.10 Natural occupation numbers $\rho_1(t)$ and $\rho_2(t)$ as a function of time for $T_{ramp} = 25, 500$ but for stronger interaction $\lambda = 0.35$ (instead of 0.1) and a logarithmic vertical scale. The case of $T_{ramp} = 25$ is qualitatively the same as seen before. For the longer time $T_{ramp} = 500$ the system lies in a "counterintuitive" regime, where the system does not evolve towards the fragmented ground state and stays coherent.

amined before in Sec 3.2.2 and Figs. 3.8 and 3.9. For a longer ramp time of $T_{ramp} = 500$ the system does, however, not tend towards a fragmented state and remains condensed, i.e., only one eigenvalue of the reduced density-matrix macroscopically. The regime where this occurs has been coined "counterintuitive" or "inverse" regime [19]. An explanation for this inverse regime is given in the paper by Streltsov et al. [19]. At the beginning virtually only the condensed ground state is populated, which remains true for slow ramp-up times. Now, after some time and at a certain barrier height, a fragmented eigenstate becomes energetically favorable, but the system cannot abruptly change its properties. This is the reason it largely remains coherent. For fast ramp-up times, however, a large enough fraction of the condensate is in an excited state, which makes it possible to evolve towards the fully fragmented ground state.

We were not able to find this inverse regime for any T_{ramp} and particle number in the potential with the interaction strength studied in the previous Sec 3.2.2 and Figs 3.8 and 3.9. The existence of the inverse regime therefore depends on the exact double-well potential considered.

Chapter 4

Summary

We have investigated the ground state of a BEC in a double-well potential by solving the many-body Schrödinger equation using the MCTDHB method. Quantities like the particle density, first and second-order coherence functions in real and momentum space, as well as the fragmentation of the system were studied. We also provided an analytical discussion of the double-well potential and the occurrence of fragmentation in such a system.

Numerically, we found four distinct regions in the studied potential, depending on the number of particles and the height of the barrier. For small barrier height there were two regions were the ground state is coherent. These regions are distinguished by the single-particle energies of the orbitals. In the third region for high barriers, the ground state is fragmented, as expected from the analytical model and previous works. The fourth region for high barriers and particle numbers was found to again be not fragmented. This is surprising, as one would expect the fragmented region to extend to arbitrary particle numbers.

For a double-well potential the first order coherence of the system is lost in the fragmented region. The second-order coherence, however, is maintained, at least for the values on the diagonal.

We studied a double-well with a time-dependent barrier. It was shown, that even for very slow ramp-up times of the order of the lifetime of a BEC, the process is not fully adiabatic. After the ramp-up, the system still exhibited oscillations of the occupation numbers, and therefore was not in the ground state anymore. If further the final state of the potential lies in the newly found coherent region for high barriers, the initial state would only evolve towards the ground state for slow ramp-up times. For fast ramp-up times the state tended towards an excited, fragmented state.

In comparison a "counterintuitive" regime is found for a different system as in Ref. [19], where the initial state does not evolve towards the fragmented ground

state for slowly increasing barriers as well. Here it rather stayed in a low-lying, condensed excited state. This is in contrast to the case where the condensate stays in the ground state for slow ramp-up times, which is coherent at all times.

Some questions still remain open. First, the numerical solution differs from the analytical solution which was provided. A better understanding of this difference would likely provide further insight on the transition of the coherent to the fragmented state, as well as why fragmentation disappears for high particle numbers. Furthermore it is possible that the inverse regime is related to the newly found coherent region, as the time-evolutions plotted in Chapter 3 have great similarities, and the interaction energy is of similar order. Lastly it would be interesting to investigate how a different than a linear ramp-up function influences the dynamics of the system.

Appendix A

Ground state

In this appendix, we collect results complementary to our findings in Sec. 3.1 of this thesis.

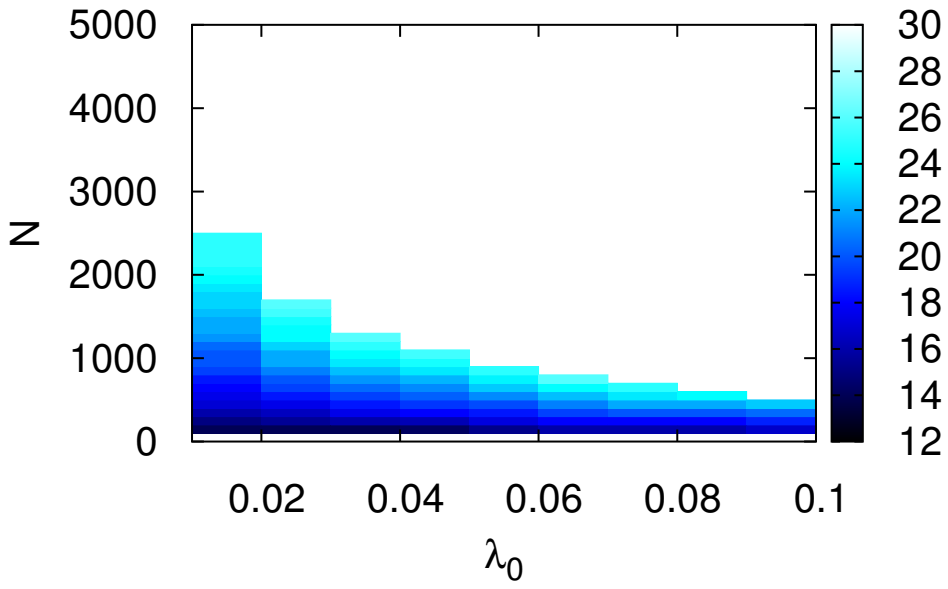

Figure A.1 Minimum barrier heights at which the excited fraction $F \geq 0.25$ as a function of the particle number N and the interaction strength λ_0. White indicates that there was no barrier height at which the exited fraction F exceeded the threshold of 0.25.

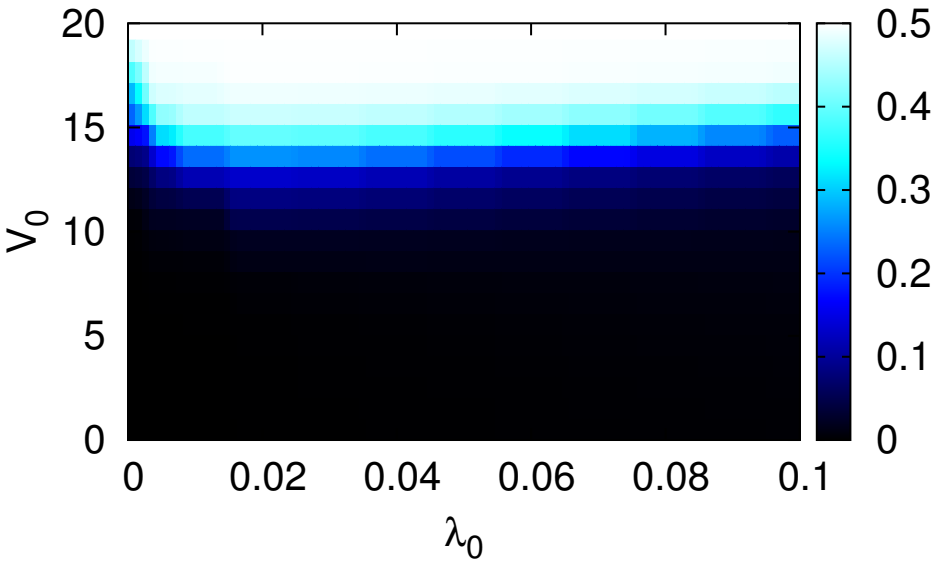

Figure A.2 The excited fraction as a function of the contact interaction strength λ_0 and the barrier height for a constant particle number of $N_{par} = 100$. Note that the minimum value of λ_0 calculated was 0.0001. For non-interacting systems (i.e.,$\lambda_0 = 0$) the fragmentation disappears ($F = 0$).

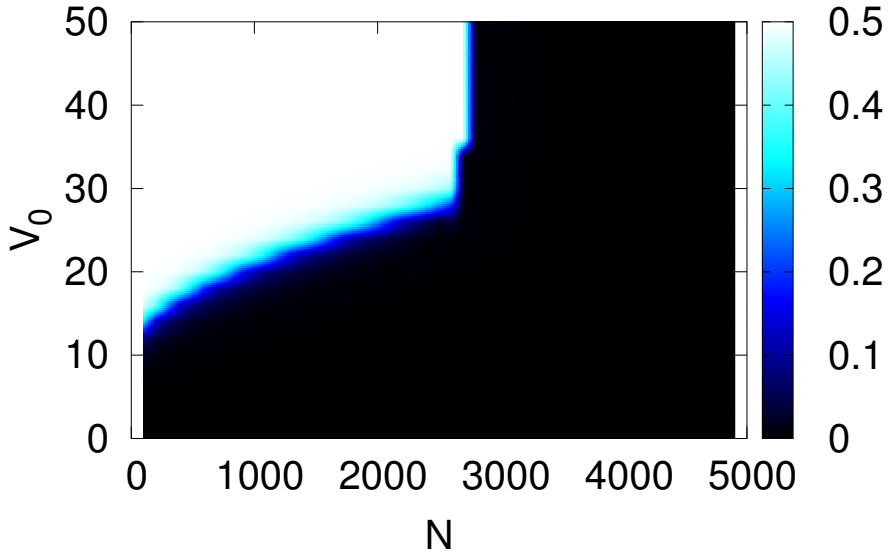

Figure A.3 The excited fraction plotted as a function of barrier height and the particle number in the same potential as in Section 3.1. The single-particle contact interaction constant λ_0 was chosen to be 0.02. Fragmentation disappears for strong mean-field interactions, even at high barriers. Note that the step at $N \approx 3000$ is caused by the low resolution of this plot. The disappearance of fragmentation appears at roughly the same mean-field interaction strength $(N-1)\lambda_0 \approx 60$ as in Fig. 3.6.

Appendix B

Dynamics

In this appendix, we collect results complementary to our investigation of the dynamics of BECs in time-dependent double-wells in Sec. 3.2 of this thesis.

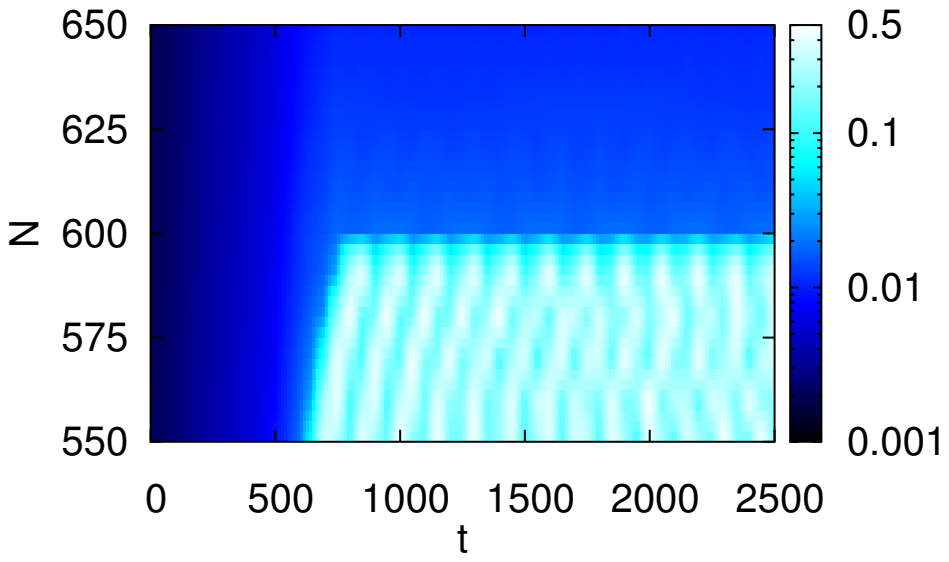

Figure B.1 Fragmentation as a function of time t for different particle numbers N, and constant $V_0 = 30$, ramp-up time $T_{ramp} = 750$ and contact interaction strength $\lambda_0 = 0.1$. For $N \geq 600$ the state remains coherent. Comparing with Fig 3.6 we find that the system therefore oscillates around the ground state for all particle numbers N, as for $N \geq 600$ the ground state is coherent. This behavior is consistent with Fig. 3.6, i.e., fragmentation also disappears in the dynamic case for slow ramp-up.

Bibliography

[1] K. Huang, *Statistical mechanics* (Wiley, 1987), ISBN 9780471815181.

[2] A. Leggett, *Quantum Liquids: Bose Condensation and Cooper Pairing in Condensed-matter Systems*, Oxford graduate texts in mathematics (OUP Oxford, 2006), ISBN 9780198526438.

[3] P. Nozières and D. Saint James, J. Phys. (Paris) **43**, 1133 (1982).

[4] O. Penrose and L. Onsager, Phys. Rev. **104**, 576 (1956).

[5] R. Jördens, N. Strohmaier, K. Günter, H. Moritz, and T. Esslinger, Nature **455**, 204 (2008).

[6] M. Greiner, O. Mandel, T. Esslinger, T. W. Hänsch, and I. Bloch, Nature **415**, 39 (2002).

[7] M. H. Anderson, J. R. Ensher, M. R. Matthews, C. E. Wieman, and E. A. Cornell, Science **269**, 198 (1995).

[8] C. C. Bradley, C. A. Sackett, J. J. Tollett, and R. G. Hulet, Phys. Rev. Lett. **75**, 1687 (1995).

[9] K. B. Davis, M. O. Mewes, M. R. Andrews, N. J. van Druten, D. S. Durfee, D. M. Kurn, and W. Ketterle, Phys. Rev. Lett. **75**, 3969 (1995).

[10] E. A. Burt, R. W. Ghrist, C. J. Myatt, M. J. Holland, E. A. Cornell, and C. E. Wieman, Phys. Rev. Lett. **79**, 337 (1997).

[11] M. Naraschewski and R. J. Glauber, Phys. Rev. A **59**, 4595 (1999).

[12] S. Zöllner, H.-D. Meyer, and P. Schmelcher, Phys. Rev. Lett. **100**, 040401 (2008).

[13] Y. Shin et al., Phys. Rev. Lett. **92**, 050405 (2004).

[14] B. V. Hall et al., Phys. Rev. Lett. **98**, 030402 (2007).

[15] A. J. Leggett and F. Sols, Phys. Rev. Lett. **81**, 1344 (1998).

[16] C. Menotti et al., Phys. Rev. A **63**, 023601 (2001).

[17] E. H. Lieb and R. Seiringer, Phys. Rev. Lett. **88**, 170409 (2002).

[18] W. Ketterle and N. J. van Druten, Phys. Rev. A **54**, 656 (1996).

[19] A. I. Streltsov, O. E. Alon, and L. S. Cederbaum, Phys. Rev. Lett. **99**, 030402 (2007).

[20] K. Sakmann, A. I. Streltsov, O. E. Alon, and L. S. Cederbaum, Phys. Rev. A **78**, 023615 (2008).

[21] O. E. Alon, A. I. Streltsov, and L. S. Cederbaum, Phys. Rev. A **77**, 033613 (2008).

[22] P. Kramer and M. Saraceno, *Geometry of the Time-Dependent Variational Principle in Quantum Mechanics* (Springer, Berlin, 1981).

[23] M. Beck, A. Jäckle, G. Worth, and H.-D. Meyer, Physics Reports **324**, 86 (2000).

[24] A. U. J. Lode, M. C. Tsatsos, and E. Fasshauer, *MCTDH-X: The time-dependent multiconfigurational hartree for indistinguishable particles software* (2016), URL `http://ultracold.org`.

[25] R. J. Glauber, Phys. Rev. **130**, 2529 (1963).

[26] R. Spekkens and J. Sipe, Fortschritte der Physik **46**, 873 (1998).

[27] R. W. Spekkens and J. E. Sipe, Phys. Rev. A **59**, 3868 (1999).

[28] C. J. Pethick and H. Smith, *Bose–Einstein Condensation in Dilute Gases* (Cambridge University Press, 2008), 2nd ed.

Acknowledgements

I would like to thank my supervisors Axel Lode and Christoph Bruder for their guidance throughout this project and providing me help whenever I needed it. I also want to thank Marios Tsatsos for his inputs.

Calculations were performed at sciCORE (`http://scicore.unibas.ch/`) scientific computing core facility at University of Basel.

Last but not least I want to thank my family for their unconditional support and encouragement.

University of Basel

Faculty of Science

Declaration on Scientific Integrity

(including a Declaration on Plagiarism and Fraud)

Bachelor's / Master's Thesis *(Please cross out what does not apply)*

Title of Thesis *(Please print in capital letters)*:

_____

_____

_____

First Name, Surname *(Please print in capital letters):* _____

Matriculation No.: _____

I hereby declare that this submission is my own work and that I have fully acknowledged the assistance received in completing this work and that it contains no material that has not been formally acknowledged.

I have mentioned all source materials used and have cited these in accordance with recognised scientific rules.

In addition to this declaration, I am submitting a separate agreement regarding the publication of or public access to this work.

☐ Yes ☐ No

Place, Date: _____

Signature: _____

Please enclose a completed and signed copy of this declaration in your Bachelor's or Master's thesis .